



Cite this: *Digital Discovery*, 2025, 4, 105

Quantitative analysis of miniature synaptic calcium transients using positive unlabeled deep learning†

Frédéric Beaupré, ‡^{ab} Anthony Bilodeau, ‡^{ab} Theresa Wiesner, ^a Gabriel Leclerc, ^{ab} Mado Lemieux, ^a Gabriel Nadeau, ^a Katrine Castonguay, ^{ab} Bolin Fan, ^{cd} Simon Labrecque, ^a Renée Hložek, ^{cd} Paul De Koninck, ^{ae} Christian Gagné^{bfg} and Flavie Lavoie-Cardinal *^{ab}

Ca^{2+} imaging methods are widely used for studying cellular activity in the brain, allowing detailed analysis of dynamic processes across various scales. Enhanced by high-contrast optical microscopy and fluorescent Ca^{2+} sensors, this technique can be used to reveal localized Ca^{2+} fluctuations within neurons, including in sub-cellular structures, such as the dendritic shaft or spines. Despite advances in Ca^{2+} sensors, the analysis of miniature Synaptic Calcium Transients (mSCTs), characterized by variability in morphology and low signal-to-noise ratios, remains challenging. Traditional threshold-based methods struggle with the detection and segmentation of these small, dynamic events. Deep learning (DL) approaches offer promising solutions but are limited by the need for large annotated datasets. Positive Unlabeled (PU) learning addresses this limitation by leveraging unlabeled instances to increase dataset size and enhance performance. This approach is particularly useful in the case of mSCTs that are scarce and small, associated with a very small proportion of the foreground pixels. PU learning significantly increases the effective size of the training dataset, improving model performance. Here, we present a PU learning-based strategy for detecting and segmenting mSCTs in cultured rat hippocampal neurons. We evaluate the performance of two 3D deep learning models, StarDist-3D and 3D U-Net, which are well established for the segmentation of small volumetric structures in microscopy datasets. By integrating PU learning, we enhance the 3D U-Net's performance, demonstrating significant gains over traditional methods. This work pioneers the application of PU learning in Ca^{2+} imaging analysis, offering a robust framework for mSCT detection and segmentation. We also demonstrate how this quantitative analysis pipeline can be used for subsequent mSCTs feature analysis. We characterize morphological and kinetic changes of mSCTs associated with the application of chemical long-term potentiation (cLTP) stimulation in cultured rat hippocampal neurons. Our data-driven approach shows that a cLTP-inducing stimulus leads to the emergence of new active dendritic regions and differently affects mSCTs subtypes.

Received 28th June 2024
Accepted 19th November 2024
DOI: 10.1039/d4dd00197d
rsc.li/digitaldiscovery

^aCERVO Brain Research Center, Québec, Canada. E-mail: flavie.lavoie-cardinal@cervo.ulaval.ca

^bInstitute Intelligence and Data, Université Laval, Québec, Canada

^cDunlap Institute for Astronomy and Astrophysics, University of Toronto, Toronto, Canada

^dDavid A. Dunlap Department for Astronomy and Astrophysics, University of Toronto, Toronto, Canada

^eDepartment of Biochemistry, Microbiology and Bioinformatics, Université Laval, Québec, Canada

^fDepartment of Electrical Engineering and Computer Engineering, Université Laval, Québec, Canada

^gCanada CIFAR AI Chair, Affiliated to Mila, Canada

^hDepartment of Psychiatry and Neuroscience, Université Laval, Québec, Canada

† Electronic supplementary information (ESI) available. See DOI: <https://doi.org/10.1039/d4dd00197d>

‡ These authors contributed equally to this work.

§ Current address: Aix-Marseille Université, CNRS, INP UMR 7051, NeuroCyto, Marseille, France.

1 Introduction

Ca^{2+} imaging is widely used for the study of cellular activity modulations in the brain, enabling detailed monitoring and analysis of dynamic processes at various scales: from large neuronal networks down to individual synapses.^{1,2} Exploiting high-contrast optical microscopy approaches and fluorescent Ca^{2+} sensors, it offers insights into localized fluctuations of Ca^{2+} concentration within neurons.^{3,4} In the last decade, the development of a variety of sensitive Ca^{2+} sensors with increased brightness and improved detection kinetics has opened up new possibilities for the monitoring of dynamic processes occurring in small cellular compartments such as dendritic spines.^{5–7} For instance, Ca^{2+} imaging of miniature Synaptic Calcium Transients (mSCTs) has been studied to monitor the NMDA-receptor driven Ca^{2+} influxes generated by the spontaneous release of glutamate-containing presynaptic vesicles.^{3,8–12} mSCTs are



characterized by wide variability in their morphology and spatio-temporal propagation, but also by a generally small difference between peak and background intensity fluctuations.³ This makes the task of selecting a robust and general method for automated mSCT analysis very challenging. Spike-inference approaches have been developed to describe the underlying process by which spiking activity leads to fluorescence measurements.^{13,14} However, such methods do not take

into account the spatial extent of calcium events and do not address the problem of event detection from raw videos. Threshold-based methods relying on the extraction of regions of interest (ROIs) have been proposed to segment cell body from whole cell Ca^{2+} imaging videos.^{15,16} Such approaches were also applied to detect small events, such as astrocytic calcium events,^{17,18} which are more similar to the task of mSCT detection. However, the accuracy of the threshold-based methods is

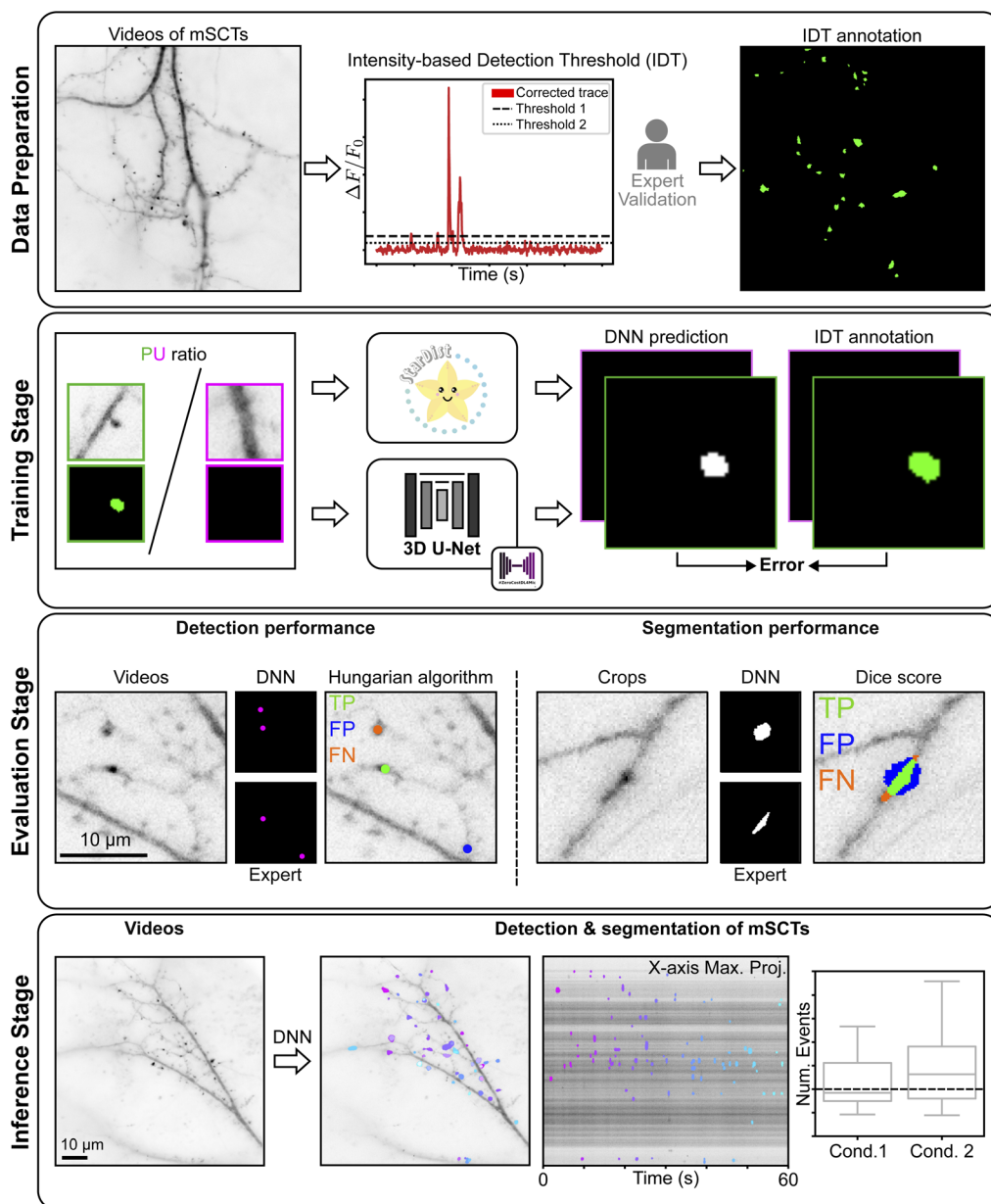


Fig. 1 Deep learning algorithm workflow. Data preparation: Ca^{2+} imaging of the fluorescent protein GCaMP6f in cultured hippocampal neurons was performed with Total Internal Reflexion Fluorescence (TIRF) microscopy. The localized fluorescent transients are segmented using an intensity-based detection threshold (IDT) approach. Detected transients are validated by an expert to differentiate between random foreground fluorescence signal fluctuations and mSCTs. Training stage: a DL model is trained on the dataset generated with the expert-validated IDT method with a PU learning scheme for automated detection and segmentation of mSCTs. Evaluation stage: crops of the model predictions and expert ground truths are compared. Detection and segmentation performance are assessed according to a weighted centroid detection error and the dice similarity score, respectively. Inference stage: the trained DL model is used to infer segmentation masks from input Ca^{2+} imaging videos containing mSCTs. Maximum projections of the input video and predicted segmented events are shown. Predicted segmentation masks of mSCTs can be used for multidimensional feature analysis.



reduced for events that propagate or change size and shape over time. Noise-based thresholding was proposed to detect and track sub-cellular events occurring at random locations and propagating over time such as mSCTs.¹⁹

While user-defined analysis pipelines are still common, the bio-imaging field has seen a shift of paradigm in the tools developed for quantitative analysis. Indeed, further performance gains can be obtained with the use of deep learning (DL) for segmentation,²⁰ small object segmentation²¹ (Ma *et al.*²² for a review), or calcium analysis^{23,24} when compared to user-defined pipelines. DL offers data-driven approaches to automatically learn features and patterns present in a dataset that define the structures or events. Consequently, these networks do not require to make *a priori* assumptions on either the regions of interest, model-based definitions of spatio-temporal features, or on parameter choices specific to a given task. They have been applied successfully to Ca^{2+} imaging detection tasks at the cellular level.^{25–27}

One limitation for the broad deployment of supervised DL-based Ca^{2+} imaging analysis is the need for large annotated datasets²⁸ to train the DL models. In many experimental contexts, including Ca^{2+} imaging, negative instances, corresponding to pixels that do not contain a Ca^{2+} event at a given time point, account for a large proportion of the image.^{29,30} This represents an additional challenge for the development of DL analysis strategies. In cases where Ca^{2+} transients (positive instances) are small and scarce, a large fraction of the foreground remains without annotation (unlabeled). Positive Unlabeled (PU) learning was proposed to harness unlabeled instances with the intuition that they can be leveraged to train deep neural networks.^{31,32} It can be used to address challenges associated with the impossibility to annotate all negative instances due to time constraints or subjectivity of the annotation process.³³ During PU training, the DL model has access to positive instances and a predefined number of unlabeled instances. This significantly increases the size of the training dataset by providing additional information to the DL models and leveraging the abundance of unlabeled data. In the context of mSCT detection, we reason that unlabeled crops contain information about random Ca^{2+} fluctuations that can be leveraged by the DL model during training to better differentiate between mSCTs and random fluctuations. PU learning has already been applied with success to several bio-image analysis tasks.^{34–36}

Here, we present a PU learning-based strategy for the analysis of mSCTs in cultured rat hippocampal neurons (Fig. 1). The approach was developed to be applicable for the detection and segmentation of mSCTs characterized by a large diversity of signal amplitudes, frequencies, and spatial distributions. Our algorithm provides both mSCT detection and segmentation through the use of spatio-temporal (2 spatial dimensions + 1 temporal dimension) DL models (3D U-Net³⁷ and StarDist-3D³⁸). We introduce PU learning in the context of mSCTs detection, using foreground intensity fluctuations as unlabeled instances and mSCTs as positive instances. In the absence of unlabeled instances for training, our algorithm is similar to that of Dotti *et al.*,³⁹ which implements a 3D U-Net for segmentation of low SNR Ca^{2+} events in full-frame confocal imaging data. The authors

tackled a multi-label instance segmentation task to differentiate between types of Ca^{2+} release in the context of cardiomyocytes. We build upon this work in an instance segmentation task and show that the addition of unlabeled instances to the training procedure leads to significant gains in the performance of the 3D U-Net. To the best of our knowledge, this is the first use of PU learning for Ca^{2+} imaging analysis. We leverage the trained DL model to create a multidimensional analysis framework, which allows the analysis of mSCT features associated with the application of a chemical long term potentiation (cLTP) inducing stimulus.

2 Methods

2.1 Neuronal cell culture

Dissociated rat hippocampal cultures were prepared as described previously.^{40,41} In brief, hippocampi were dissected out of P1 rats, following approved protocols from the Université Laval animal care committee, dissociated enzymatically (papain, 12 U/ml; Worthington), and mechanically (trituration through Pasteur pipette). After dissociation, the cells were washed, centrifuged, and plated on poly-D-lysine-coated glass (18 mm) coverslips at a density of ~67 500 cells per mm². Growth media consisted of Neurobasal and B27 (50 : 1), supplemented with penicillin/streptomycin (50 U/ml; 50 μg ml⁻¹) and 0.5 mM L-glutamax (Invitrogen). Fetal bovine serum (2%; HyClone) was added at time of plating. After 5 days, half of the media was changed without serum and with Ara-C (5 μM ; Sigma-Aldrich) to limit proliferation of non-neuronal cells. After that, half of the growth medium was replaced with serum- and Ara-C-free medium twice a week. For Ca^{2+} imaging, neurons were transfected with GCaMP6f-expressing plasmid (pGP-CMV-GCaMP6f)⁶ using Lipofectamine 2000 (Invitrogen). For the plasticity experiments, neurons were transfected at day *in vitro* (DIV) 9–13 and imaged 24 h later. For the generation of the training dataset for the detection and segmentation of mSCTs, videos from neurons imaged at DIV 7–17 were included.

2.2 Imaging solutions and pharmacology

The HEPES-buffered aCSF solution used for Ca^{2+} imaging contained: 104 mM NaCl, 5 mM KCl, 10 mM Na-HEPES, and 10 mM glucose. To initially maintain little or no NMDA receptor activity during the transfer of the coverslip to the microscope, this solution contained 0.6 CaCl_2 and 5.0 MgCl_2 (high- Mg^{2+} -aCSF). For mSCT measurements, the solution was adjusted to contain no Mg^{2+} , 1.2 mM Ca^{2+} and 0.5 μM Tetrodotoxin (TTX, Alomone Labs) (0Mg²⁺/TTX-aCSF). For chemical long term potentiation (cLTP) stimulation, the aCSF solution without Mg^{2+} was supplemented with 0.2 mM glycine and 0.01 mM bicuculline (0Mg²⁺/Gly/Bic-aCSF).⁴² The osmolarity of every solution was maintained around 230 Osm, close to the neurobasal-based growth media value of the neuronal cell cultures.

2.3 Live imaging and plasticity protocol

Neurons were imaged using a 100x 1.49NA immersion objective on an inverted Olympus IX-71, equipped with a TIRF



illuminator, set on an oblique illumination mode to detect fluorescence with improved contrast.⁴³ The microscope was equipped with a multi-valve perfusion system (VC3-8xG, ALA Scientific instruments) and an inline heater (SF-28, Warner) so that neurons were continuously perfused with heated (32 °C) solutions. Transfected neurons were imaged with a Toptica iChrome MLE laser at 488 nm. GCaMP6f fluorescence emission was filtered through a Semrock, Brightline 520/35 cube placed before the objective and recorded on a Charge-coupled device (CCD) camera (Princeton ProEm 512B-FT) at a rate of 10 frames per second. The pixel size was 0.16 μm. Image acquisition was performed using a custom written Matlab script in Matlab2007 (ref. 43).

For the generalization experiment of the trained model, time-lapse imaging of GCaMP6f was performed at room temperature using an upright microscope (Axioskop FS2; Zeiss) equipped with a 63x 0.95 NA Achroplan water immersion objective (Zeiss) and a multivalve perfusion system (PTR-2000; ALA Scientific Instruments). Fluorescence excitation was achieved using a Lambda DG-4 system with a 175 W Xenon lamp (Sutter Instrument), using a 485/20 nm excitation filter and a LP515 emission filter. Images were acquired in epifluorescence mode with an EMCCD camera (QuantEM:512SC; Photometrics) using an exposure time of 150 ms and a 2 × 2 binning.

For the mSCT plasticity experiments, neurons were transfected at DIV 9–13 and imaged 24 h later. Coverslips were first transferred from the incubator to the perfusion chamber containing fresh high-Mg²⁺-aCSF, to block the activity and prevent any cellular stress. The perfusion was switched for the imaging session to 0Mg²⁺/TTX-aCSF and a baseline Ca²⁺ imaging video of 600 frames (60 seconds) was acquired. Immediately after, the perfusion was changed to 0Mg²⁺/Gly/Bic-aCSF for 7 minutes for the cLTP stimulation. After the 7 min cLTP stimulation, the perfusion was switched back to 0Mg²⁺/TTX-aCSF solution. For the control condition, neurons were kept in the 0Mg²⁺/TTX-aCSF throughout. Neurons were not imaged during the cLTP stimulation to prevent photobleaching of the Ca²⁺ sensor. Directly after the stimulation, the perfusion was switched back to 0Mg²⁺/TTX-aCSF. For both conditions a baseline Ca²⁺ imaging video was first acquired followed by a second video, starting 10 min after the end of the baseline. During the acquisition of both Ca²⁺ imaging videos the solution was 0Mg²⁺/TTX-aCSF.

2.4 Intensity-based detection threshold (IDT) annotator

We developed an intensity-based detection threshold (IDT) algorithm to detect and segment mSCTs while recording their temporal and spatial position. IDT is implemented in Matlab 2018 (Mathworks Inc., Natick, USA). It consists of 3 phases: (i) data preprocessing, (ii) automated detection and segmentation of mSCTs, and (iii) manual verification of the detected Ca²⁺ events.

Acquired streams were initially aligned in *x* and *y* to the first frame of the video using the custom written Matlab code of Guizar-Sicairos *et al.*⁴⁴ Subsequently, the background noise was removed by manually choosing a region of interest in the

background and by subtracting its average intensity from each frame. To detect the foreground, a spatial median filter was applied (kernel size of 3) and manual adjustment of an intensity-based threshold was performed. Ca²⁺ transient detection was performed pixel-wise from the foreground mask. For each pixel the fluorescence intensity was extracted and the baseline was corrected using asymmetric re-weighted penalized least square algorithm (arPLS).⁴⁵ The fluorescence signal *F* was normalized to the baseline fluorescence *F*₀ with:⁴⁶

$$\Delta F/F_0 = \frac{F - F_0}{F_0}. \quad (1)$$

To identify real Ca²⁺ events from fluorescence foreground fluctuations, we first evaluated the noise of the baseline fluorescence trace. We compared the standard deviation (STD) of the signal while iteratively excluding the time points with the highest values, which correspond to Ca²⁺ events rather than noise fluctuations. When the STD between 2 consecutive iteration steps becomes similar, indicating that most of the Ca²⁺ events have been removed, we use the measured STD as an approximation of baseline noise fluctuations for subsequent steps. Ca²⁺ transients are detected with the Matlab function *findpeaks*. The first threshold is used to detect peaks in the baseline corrected time traces and set at 4 × STD (detection threshold). A second threshold of 2 × STD is applied subsequently and used for the segmentation of the mSCTs (segmentation threshold). The segmentation threshold is applied within a time window of 1500 ms before and after the peak to determine the length of the mSCTs. Using this approach, events lasting only 1 frame are discarded.

The spatial and temporal properties of the segmented objects are calculated using the *regionprops* function in Matlab. The events having one of their spatial axis ≤ 3 pixels are removed. Following this first automated detection step, the user is asked to verify each detected event with the help of a graphical user interface (GUI). The GUI displays a small crop centered around each event (64 by 64 pixels, 12 frames), the corresponding baseline-correction, and detection of the normalized Ca²⁺ transients. In the GUI, the user inspects the detected events to determine which ones correspond to mSCTs and should be kept for future analysis. To facilitate the analysis, events detected at different time points but with weighted centroids closer than 2.55 μm are given the same region identifier (ID) and can be proofed at the same time. We noted that mSCTs which occur at a high frequency at the same position are often missed by IDT. Additionally those segmented events typically last longer than 4.5 seconds. This issue arises from defining the end of an event as the fluorescence signal dropping below the second threshold, particularly during bursts of events. Hence, the user is asked to inspect these events with another GUI showing the mSCT (64 by 64 pixels, 12 frames) and the overlapped segmentation at the maximal peak intensity frame. This is required to extract the total number of events but does not affect the mask of IDT used to train the DL models. The analysis time of a video strongly depends on the number of Ca²⁺ transients. On average we can find between 100–800 events and



the analysis of such videos can require from 2 to 4 hours (automated and manual steps combined).

2.5 Dataset

The training dataset consisted of 14 Ca^{2+} imaging videos acquired on different neurons. To account for the very small size of the training dataset, we measured the averaged performance of each model trained with five independent random seeds and five distinct groups of 14 Ca^{2+} imaging videos annotated using the IDT algorithm. Positive crops ($64 \times 64 \times 64$ pixels) were generated for each transient detected by IDT and manually validated by an expert. For each subset, unlabeled crops were sampled from the foreground to obtain the desired PU ratio. Unlabeled crops from a smaller PU ratio are a subset of the next PU ratio, *e.g.* the set of unlabeled crops used to train the models with a PU ratio of 1–2 is contained in the set of unlabeled crops used to train the models with a PU ratio of 1–4. The validation dataset was kept constant for all training and consisted of 15 independent Ca^{2+} imaging videos that were annotated with the IDT algorithm.

The testing detection dataset consisted of 10 independent Ca^{2+} imaging videos that were manually annotated by an expert at the peak intensity of the mSCT. The manual detection of mSCTs consisted of point annotations of the event centroids at the maximal $\Delta F/F_0$ frame. The segmentation testing dataset consisted of manual segmentation masks obtained from two experts for 69 mSCTs of varied size, shape, and intensity. The masks were drawn on (32×32 pixels) pixel crops centered on the frame with maximal $\Delta F/F_0$ for each mSCT. This was required to reduce the impact of missed events (false negatives) and the imprecise segmentation masks from the IDT algorithm during the evaluation.

2.6 DL models

All DL models were trained on crops of size ($32 \times 32 \times 32$) from the aligned and normalized version of the acquired Ca^{2+} imaging videos (baseline correction and $\Delta F/F_0$, see 2.4) and the corresponding IDT annotations. Training parameters varied for both models and are described below. At inference, tiles of size ($64 \times 64 \times 64$) are used to make the final prediction.

2.6.1 3D U-net. A modified 3D U-Net was implemented³⁷ in PyTorch.⁴⁷ The encoder part of the architecture consisted of 5 layers of double convolution blocks followed by max pooling with a kernel size and stride of 2. The number of filters was doubled after each layer (8, 16, 32, 64, 128). Throughout the model, a kernel size of 3 with zero-padding and a stride of 1 were used. After each convolution, a batch normalization layer and leaky ReLU (0.02) were used. The bottleneck of the model consisted in two convolution layers, each followed by a ReLU activation. For the decoder part, features from lower layers were upscaled using transposed convolutions and concatenated with the information obtained from the skipping links located at the same depth. This was followed by a double set of convolution, batch normalization and ReLU. A final convolution layer projected the information to a single channel prediction and was followed by a sigmoid function.

The model was trained with the Adam optimizer, with default parameters and a learning rate of 0.0002, to minimize the mean quadratic error. The model was trained for 100k steps with a batch size of 128. Every 100 steps, the complete validation dataset was used to assess the generalization performance. Random crops and spatial flip were used during training for data augmentation. The model with the best performance on the validation test was kept for testing.

2.6.2 StarDist-3D. We used the default implementation from ref. 38 and 48. In brief, the StarDist approach proposes to localize objects of interest *via* star-convex polygons. More specifically, the StarDist method trains a 3D U-Net architecture to predict object probabilities as well as star-convex polygons parameterized by the distances to object boundaries. These predictions produce a set of candidate polygons for a given input image, after which a final result is obtained *via* non-maximum suppression (NMS) of the candidates.

The model was trained for 400 epochs with a batch size of 64 and 100 batches per epochs. The same data augmentation technique to the 3D U-Net was used during training.

2.6.3 UNetR and Attention-UNet. We used the UNetR⁴⁹ model implementation from the MONAI library with default parameters.⁵⁰ For Attention-UNet,⁵¹ we also used the model implementation from the MONAI library. We set the number of channels at each layer to 16, 32, 64, 128, 256 and used a stride of 2. Other parameters were set to their default values.

The models were trained with the Adam optimizer, with default parameters and a learning rate of 0.0002. The models were trained with their recommended loss function (DiceCE loss: a weighted sum of the dice loss and the cross-entropy loss) or with the mean squared quadratic loss function. In all cases, the models were trained for 100k steps with a batch size of 128. Every 100 steps, the complete validation dataset was used to assess the generalization performance. Random crops and spatial flips were used during training for data augmentation. The model with the best performance on the validation test was kept for testing.

2.7 Positive unlabeled learning

Typical supervised DL algorithms learn to represent data using raw inputs and their corresponding annotations.⁵² A binary classification problem consists in training a model to discriminate two classes of events (*e.g.*, positive and negative). Traditionally, supervised machine learning makes use of a dataset $\{(\mathbf{x}_0, y_0), (\mathbf{x}_1, y_1), \dots\}$ where $\mathbf{x}_i \in \mathbb{R}^D$ is the input and y_i , the associated annotation. In the case of the detection task we have $y_i \in \{0, 1\}$, with the sample being positive when $y = 1$ and negative otherwise ($y = 0$).

In Positive Unlabeled (PU) learning,³¹ a binary variable $s \in \{0, 1\}$ on whether an example was annotated or not is introduced in the training dataset $\{(\mathbf{x}_0, y_0, s_0), (\mathbf{x}_1, y_1, s_1), \dots\}$. When the annotation process does not make annotation errors, it implies that $P(y = 1|s = 1) = 1$. When $s = 0$, then the example can belong to both classes.

In some fields, such as biomedical imaging, deep learning algorithms can be difficult to implement due to the scarcity or



cost of acquiring data belonging to the positive class, or label.⁵³ In this study, mSCTs account for a very small portion of the training dataset (<0.05% of total pixels, or <0.3% of foreground pixels). In a PU learning framework the network learns from positive (mSCTs detected with IDT) and unlabeled examples (extracted from the foreground). Unlabeled examples differ from negative examples as they could be a positive or negative instance, albeit with a much larger chance of belonging to the negative class for very sparse and small events such as mSCTs. Consequently, PU learning is particularly appealing and efficient when unlabeled examples are available at low cost and in large quantities.³¹

In our imaging dataset, mSCTs are the positive samples, and to construct a PU learning dataset, we sample regions along dendrites where no mSCTs were detected with IDT. As mSCTs account for such a small portion of the total video pixels, we can acquire unlabeled crops in large quantities. To better study the effect of the number of unlabeled crops on model performance, we first evaluate the performance of a model trained in a positive-only context (PU ratio 1–0). Both StarDist-3D and 3D U-Net are trained in a PU learning setting, with PU ratios ranging from 1–1 to 1–256.

2.8 Evaluation strategies

2.8.1 Detection. To assess the detection performance of the DL models, we frame the evaluation as a linear assignment problem which we solve using the hungarian algorithm⁵⁴ and the *linear_sum_assignment* function from the Python library Scipy. The hungarian algorithm aims to assign elements from group A to elements from group B while minimizing the cost of assignment. In our case, the elements of groups A and B are the centroids of the model and ground truth segmentations, and the cost of assignment is defined as a distance metric (euclidean) between the centroids. We define a value of 6 pixels as the maximum distance for a possible assignment. The performance is evaluated on the detection testing dataset consisting of 10 videos in which the centroids of all mSCTs were identified by an expert. We identified true positives (TP), false positives (FP) and false negatives (FN) with 100 evenly spaced thresholds in the interval [0.0, 1.0], which allowed computation of recall and precision scores for IDT, StarDist-3D and 3D U-Net. We also compute the average precision (AP) of every DL model for a more concise report of performance. The AP metric is defined as:

$$AP = \sum_n (R_n - R_{n-1})P_n \quad (2)$$

where P_n and R_n are the precision and recall at the n th threshold. Detection accuracy, recall and precision were also evaluated for different groups of event $\Delta F/F_0$. mSCT events were placed into 0.5 $\Delta F/F_0$ bin increments (except for the last bin which groups all events with $\Delta F/F_0 > 3$). The aforementioned metrics were computed for each bin, resulting in the matrices shown in Fig. 3g. All detection results are averaged over the 25 effective training repetitions described in the Dataset section.

2.8.2 Segmentation. The segmentation performance of the DL models is reported as the dice similarity score⁵⁵ between the model's binarized predictions and the ground truth segmentation obtained from the testing segmentation dataset. To measure intra-expert agreement, the same segmentation task was performed by experts on the testing dataset twice, with a two-week delay between annotation sessions. To measure inter-expert agreement, we compared the annotations from both experts in their first annotation session. Expert agreement was also measured using the dice similarity score. Considering that the annotations from expert 2 were in better agreement with IDT and in turn with the networks' annotations, we used expert 2's annotations as the segmentation performance of the models for different PU ratios (Fig. 4c). We considered a model better than inter-expert level when it had a dice value at peak distribution density higher than that of the inter-expert distribution (gray vertical lines in Fig. 4b). We opted for this definition rather than the distribution mean because of the double penalty that is being forced upon models which miss a large number of events (many false positives). Explicitly, models are being penalized twice on missed events; once in detection and once again in segmentation with a dice score of 0. This causes many models (especially for StarDist-3D) to show a bimodal dice score distribution with first mode near zero, which skews the distribution mean towards lower values. In contrast, experts were only shown frames displaying a mSCT, *i.e.*, they could never be penalized for a missed event, and therefore do not exhibit this bimodal dice score distribution in their agreement.

2.9 Multidimensional analysis

2.9.1 Identification of mSCT subtypes. The mSCT subtypes are identified using the K -means algorithm. The number of subtypes ($K = 5$) is obtained from the Silhouette score⁵⁶ and the Elbow method,⁵⁷ which find the optimal number of subtypes by computing the value of K at which the Silhouette score is maximal and the Elbow method exhibits a linear decreasing trend with increasing number of subtypes (ESI Fig. 5†). More specifically, K -means is performed on the dataset $X \in \mathbb{R}^{N \times M}$, where N is the number of detected mSCTs and M is the number of features characterizing the mSCTs (note that these are manually defined, ESI Table 2†).⁵⁸ Each detected mSCT is associated with its closest subtype using the pairwise euclidean distance between the averaged feature vectors of the subtypes and the feature vector of each mSCT.

2.9.2 Determination of event categories. We determined event categories using the spatial coordinate of the segmentation masks. We can associate mSCTs occurring in the same region at different time points and classify them as: Silenced (S) when they are present only in the baseline video, New (N) for events detected only after the stimulus, and recurrent (R) for events detected in the same region before (R_b), and after (R_a) the stimulus. A baseline event is considered recurrent when its weighted centroid is within 6 pixels (spatially) from an event detected in the second movie.



2.9.3 Association of recurrent events. In Fig. 5g, we associated the subtypes of recurrent baseline events R_b with the subtypes of their corresponding events detected after the cLTP stimulation R_a . The colormap of the association matrix corresponds to the percentage of R_b events of a given subtype that were associated with a specific subtype R_a .

2.9.4 Feature-based classification of mSCTs. We trained a decision tree on a binary classification task to assign mSCTs to distinct categories (silenced, recurrent, new) based on their features. The implementation from Pedregosa *et al.*⁵⁹ was used. The hyper-parameters of the decision tree are given in ESI Table 5.† For each binary classification we used 70% of events for training and 30% for testing.

We computed the features with the most impact on the classifier's predictions using SHapley Additive exPlanations (SHAP) values, which is a game theory approach used to explain the output of machine learning models.⁶⁰ SHAP values give information regarding the contribution of each feature of the mSCT to the classifier prediction. The SHAP values predict how the machine learning model would perform with and without each specific feature to discriminate between the different mSCT categories, giving insights into the most important features to distinguish, for example, mSCTs detected only prior (silenced) or after (new) the cLTP simulation.

In Fig. 5h, we plot the SHAP value for each event in the testing dataset, color-coded by their normalized feature values. The grey line corresponds to a SHAP value of 0, indicating no preference towards either class. Higher (or lower) SHAP values correspond to a greater influence on the model's output. The SHAP values are arranged according to their distribution spread, with a larger spread indicating greater importance of this feature in the decision tree prediction. The color-coding of the events highlights the relationship between the value of each feature and its impact on the model's prediction.

2.9.5 Statistical analysis. The statistical difference for the fold change difference was tested using the Wilcoxon Signed Rank Test,⁶¹ which compares the distribution of differences between two observations and tests for the median of zero, rather than the *t*-test which uses the mean and would produce a different result if the distribution of distances was non-Gaussian, which we test for using the Shapiro-Wilk statistical test.⁶² Otherwise, a *t*-test was used to determine the statistical significance. Points were considered as outliers and were discarded when they were $1.5 \times \text{IQR}$ (interquartile range) away from the median.

The statistical difference between the proportion of subtypes was computed using the χ^2 statistical analysis followed by a post-hoc χ^2 analysis test.

3 Results

3.1 Intensity threshold-based detection of mSCTs

Ca^{2+} imaging was performed with video microscopy of cultured rat hippocampal neurons transfected with a genetically-encoded Ca^{2+} indicator (GCaMP6f),⁶ using a TIRF microscope set in the oblique illumination mode.⁴³ To reveal mSCTs, the neurons were perfused with HEPES-buffered artificial

cerebrospinal fluid (aCSF) lacking Mg^{2+} and supplemented with 0.5 μM Tetrodotoxin (TTX) to block action potentials. The localized transient changes in Ca^{2+} concentration, triggered by spontaneous release of glutamate and Ca^{2+} influx through NMDA receptors were monitored in proximal dendrites (Fig. 2a-c). Videos of 60 s were acquired using a sampling frequency of 10 Hz. Lateral drift and background corrections were first applied to the raw videos (see Methods). The fluorescence signal F was normalized to the baseline F_0 ($\Delta F/F_0$, see Methods).⁴⁶

We developed an intensity-based detection threshold (IDT) approach for the detection and segmentation of mSCTs in the baseline-corrected dataset. We adopted a two-threshold approach to automatically detect and segment mSCTs in the Ca^{2+} imaging videos (Fig. 2d), followed by manual inspection of the detected events. The first threshold (4 standard deviations (STD) above the baseline noise) was used to detect transients at their maximal $\Delta F/F_0$ value, while the second threshold ($2 \times \text{STD}$) was used to generate a segmentation mask covering the entire duration of the mSCT (see Methods). A manual validation step of the detected transients was essential to confirm the detection results, as most mSCTs had a maximal $\Delta F/F_0 < 1$, making it difficult to distinguish real events from foreground fluorescence signal fluctuations using a fully-automated threshold-based approach (Fig. 1 – Data preparation). This manual step limited the number of false-positive detected events associated with noise and background fluctuations that were included in the final annotated IDT-dataset.

3.2 Detection of mSCTs with PU-learning

We used the manually curated IDT-annotated dataset of Ca^{2+} imaging videos as the ground truth to train the DL models in a supervised setting to automatically detect and segment mSCTs. The training sets consisted of 5 sets of 14 videos. The validation set included 15 annotated Ca^{2+} imaging videos. The detection performance was evaluated on a test set consisting of 10 Ca^{2+} imaging videos in which the x, y, t coordinates of the brightest point for all mSCTs were manually annotated by an expert. Manual annotation of the test set was necessary to overcome the lower detection accuracy of IDT for transients with a $\Delta F/F_0 \leq 1$. To leverage the spatio-temporal dynamics of mSCTs, we chose 3D deep neural networks that are well established in the field of microscopy: 3D U-Net³⁷ and StarDist-3D.³⁸ The 3D U-Net was implemented in the ZeroCostDL4Mic standard⁶³ and is available for the community.¶ For StarDist-3D, we used the seminal implementation.^{38,48} Both of these DL models are trained to minimize the squared error (mean squared error loss) between their prediction and the corresponding IDT annotations (see Methods). We also trained two more complex models: the UNetR⁴⁹ and the Attention-UNet.⁵¹ We first used the DiceCE Loss (weighted sum of the dice loss and the cross entropy loss) as in the seminal implementations of those models (from the MONAI library⁵⁰). We found that the precision of both models was very low due to a large number of false positives (ESI Fig. 1†). Using the mean-squared error, as for the 3D-UNet and StarDist-3D, we

¶ <https://github.com/FLClab/Calcium-Analysis>.



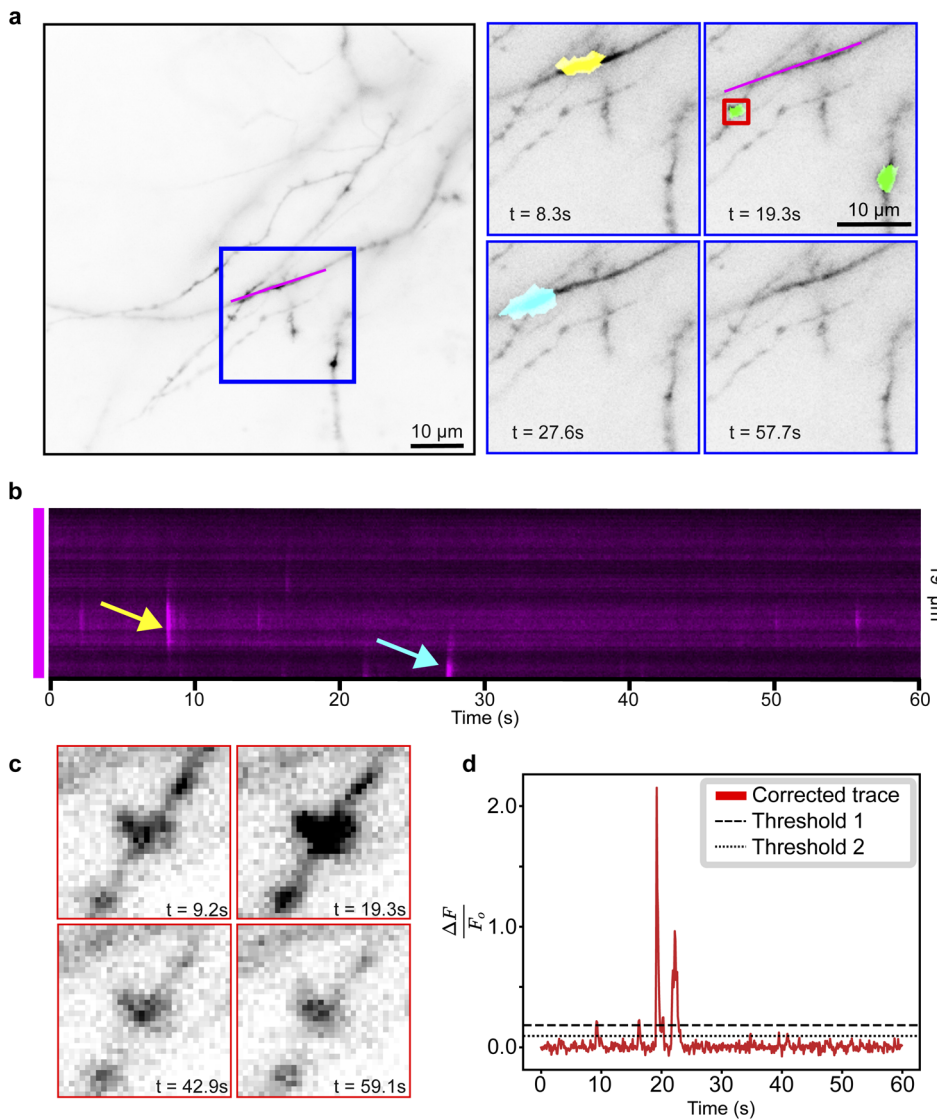


Fig. 2 Video-microscopy of mSCTs. (a) Left: maximum projection of Ca^{2+} imaging video of GCaMP6f in cultured dissociated hippocampal neurons acquired on a custom-built TIRF microscope in oblique illumination mode. Right: inset (blue square) highlighted in the left image of the full field of view at different time points. The yellow, green, and cyan regions in the insets are mSCTs detected by the IDT method. (b) Kymograph of the dendritic region delimited by the magenta line in (a). The arrows point to the events segmented in the top-left (yellow) and bottom-left (cyan) sub-region from (a). (c) (Left) Detected fluorescence signal measured at different time points for the highlighted region (red box) from the top right inset of panel a. (d) Raw and baseline Ca^{2+} traces for the mSCT shown in (c). IDT is based on two thresholds, for peak detection (threshold 1) and for transient segmentation (threshold 2).

improved the precision of UNetR and Attention-UNet but the performance remained significantly lower than that of the 3D U-Net and StarDist-3D (ESI Fig. 1†). We therefore only use the latter two for the PU experiments. To improve the DL models' ability to differentiate between fluorescence signal fluctuations and mSCTs, we included in the training set unlabeled (U) foreground regions in addition to the positive (P) annotations obtained with IDT. We introduced a variable number of unlabeled instances to the training dataset (Fig. 3a) to measure the impact of learning from unlabeled instances and validate the benefit of PU learning for a small data regime.

The detection performance of the models trained with different PU ratios is compared using precision-recall (PR) curves

(Fig. 3b and c) to quantitatively evaluate the impact of leveraging unlabeled instances during training. For each PU ratio, the DL models were trained with 25 effective folds (5 seeds for 5 different positive-unlabeled training datasets – see Methods) and the averaged performance is reported. We apply the PU learning scheme by sampling unlabeled foreground instances to generate PU ratios ranging from 1–1 to 1–256. With the 3D U-Net, we observe maximal detection performance for a PU ratio of 1–64, after which the performances decreases, albeit remaining higher than the training scheme without unlabeled instances (ratio 1–0) (Fig. 3b). For StarDist-3D, increasing the number of unlabeled instances negatively impacts its performance (Fig. 3c). For PU ratios < 1 –4, StarDist-3D shows a better performance than the 3D

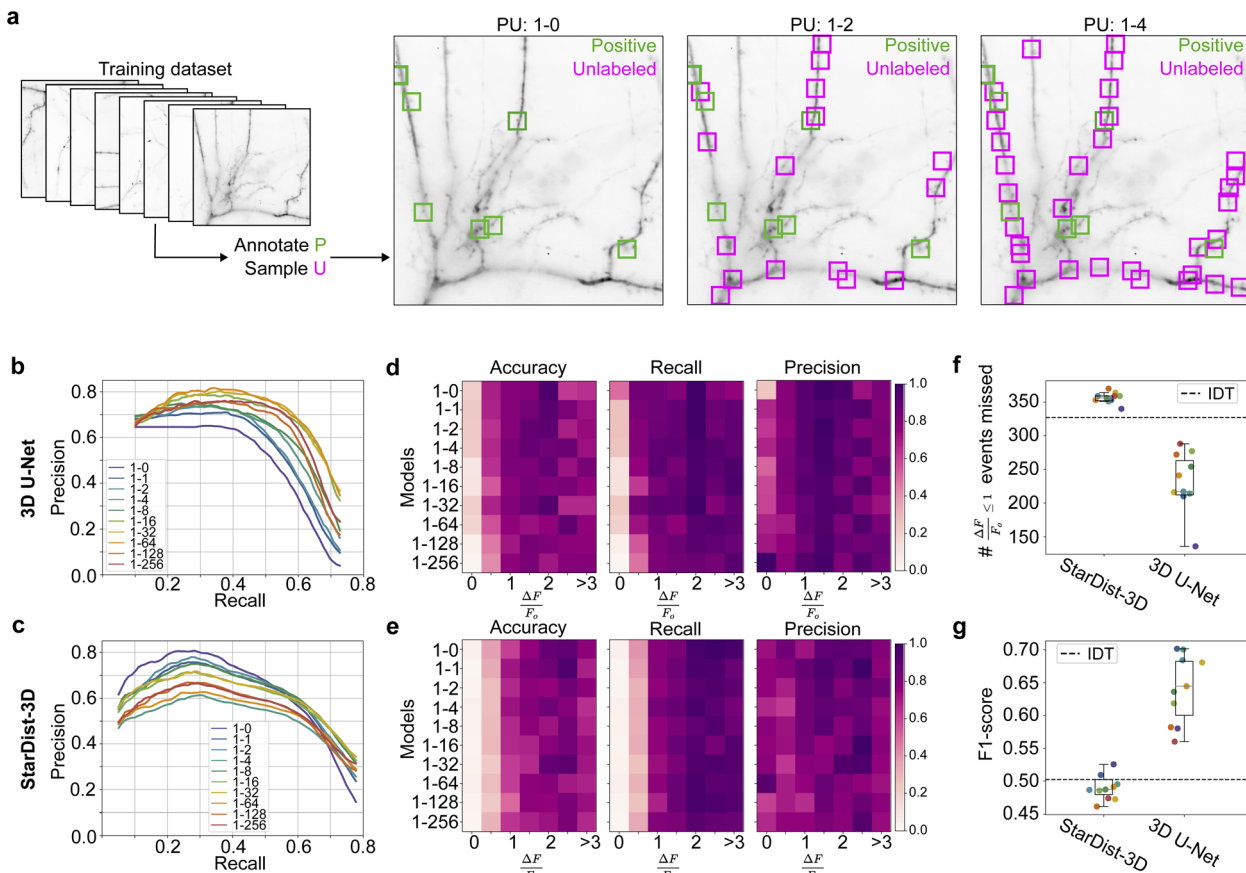


Fig. 3 Detection of mSCTs with PU learning. (a) The PU learning training dataset consists of 14 Ca²⁺ imaging videos in which mSCTs were labeled with IDT (positive instances). Unlabeled instances are sampled in each video of the training set according to the desired PU ratio. A maximum projection of a video is shown with an example of positive and unlabeled instances resulting from three different PU configurations. (b and c) 3D U-Net (b) and StarDist-3D (c) precision-recall curves for the different PU ratio. The 1-0 configuration corresponds to the dataset without unlabeled instances. (d and e) Accuracy, recall, and precision of the different 3D U-Net models (d) and StarDist-3D (e) as a function of detected events' $\Delta F/F_0$. (f) Number of events with a $\Delta F/F_0 \leq 1$ missed by each model. (g) F_1 -score of the different models, using a detection threshold optimized on the validation set in the case of StarDist-3D and 3D U-Net. (f and g) Color-coding of the data points corresponds to the different PU configurations for StarDist-3D and 3D U-Net shown in (c).

U-Net in terms of average precision (AP – see Methods). However, the 3D U-Net surpasses StarDist-3D for ratios above 1–4. Furthermore, the best 3D U-Net models (1–16, 1–32, 1–64, and 1–256) outperform the best StarDist-3D model in terms of AP, reaching a value of 0.59 for the 3D U-Net trained with a PU ratio of 1–64 (ESI Table 4†).

We then investigated the relationship between detection performance and mSCT fluorescence intensity (Fig. 3d and e). Generally, mSCTs that are most difficult to distinguish from other fluorescence signal fluctuations are small and dim ($\Delta F/F_0 < 1$). These account for the majority of the events annotated by the expert in our testing dataset (ESI Fig. 2†). As expected, the performance (accuracy, recall and precision) of the 3D U-Net and StarDist-3D increases with increasing mSCT intensity, stabilizing for $\Delta F/F_0 > 1$ for all PU ratios (Fig. 3d and e). The 3D U-Net shows an improved accuracy and recall over StarDist-3D for $\Delta F/F_0 < 1$ mSCTs (Fig. 3d and e). For the 3D U-Net, PU learning increases the precision at the cost of a small decrease in recall for PU ratios above 1–64. Training the 3D U-Net with unlabeled crops results in stricter models (better precision/

fewer false positives; see ESI Fig. 3†). This could be explained by the capability of the 3D U-Net to leverage information from unlabeled instances to refine its decision boundary between real mSCTs and foreground signal fluctuations. Fig. 3f shows that the 3D U-Net misses fewer $\Delta F/F_0 < 1$ events than the IDT annotation method (black horizontal dashed line) and StarDist-3D. Similarly the 3D U-Net performs better than IDT and StarDist-3D in terms of F_1 -score for the detected mSCTs regardless of their $\Delta F/F_0$ (Fig. 3g, see Methods).

As a last experiment, we validated whether the 3D U-Net model would generalize to an out-of-distribution dataset. This dataset consisted of Ca²⁺ imaging movies of mSCTs in cultured hippocampal neurons but was acquired on a different microscope and using different experimental conditions (Methods, ESI Fig. 4†). The mSCTs detected by the 3D U-Net trained with different PU ratios were compared with manual expert annotations of mSCTs on 5 Ca²⁺ imaging videos. The detection performance of the 3D U-Net was not impacted when tested on this dataset and improved with the PU ratios up to 1–64, after which the performance slightly decreases. This shows PU learning can

be leveraged to detect Ca^{2+} events in out-of-distribution datasets without fine-tuning of the 3D U-Net model.

3.3 Segmentation of mSCTs

Accurate segmentation of mSCTs is important for the extraction of meaningful morphological (e.g. volume, area, shape) and kinetic (e.g. duration, frequency) features from the segmented fluorescence transients. We therefore evaluated the segmentation performance of our deep neural networks (across the same PU configurations as in Section 3.2) according to the dice similarity score.⁵⁵ A dice score of zero indicates no overlap and a dice score of unity indicates total overlap. To obtain segmentation ground truths, we asked two experts to manually annotate single frames of 69 mSCTs (see Methods). The type of events that were annotated by the experts varied in form, shape, and intensity. They included synaptic, dendritic, and out-of-focus events. Moreover, the annotation was performed by the same experts at two separate time points, to assess intra- and

inter-expert agreement. Fig. 4a shows the agreement results in terms of the dice score as well as the model performance when using either expert as ground truth. We first observe that expert 1 and expert 2 show similar levels of intra-expert agreement, with minimum mSCT segmentation dice scores of 0.42 and 0.36, respectively, means of 0.77 and 0.76, and maximums at 0.91 and 0.92. The inter-expert agreement values are lower, with minimum agreement between the two experts of 0.29, mean of 0.63, and maximum of 0.93. The rather low inter-expert mean dice score highlights the ambiguous nature of ground truths in bio-imaging datasets. These low agreement values suggest that the benchmark performance against which to compare the performance of the deep neural networks is better defined as the inter-expert level of agreement rather than a perfect dice score of 1. When comparing the segmentation performance of the DL models for different PU ratios (Fig. 4b-d), we observe a slightly improved segmentation performance for the 3D U-Net compared to the inter-expert agreement for ratios below 1–64.

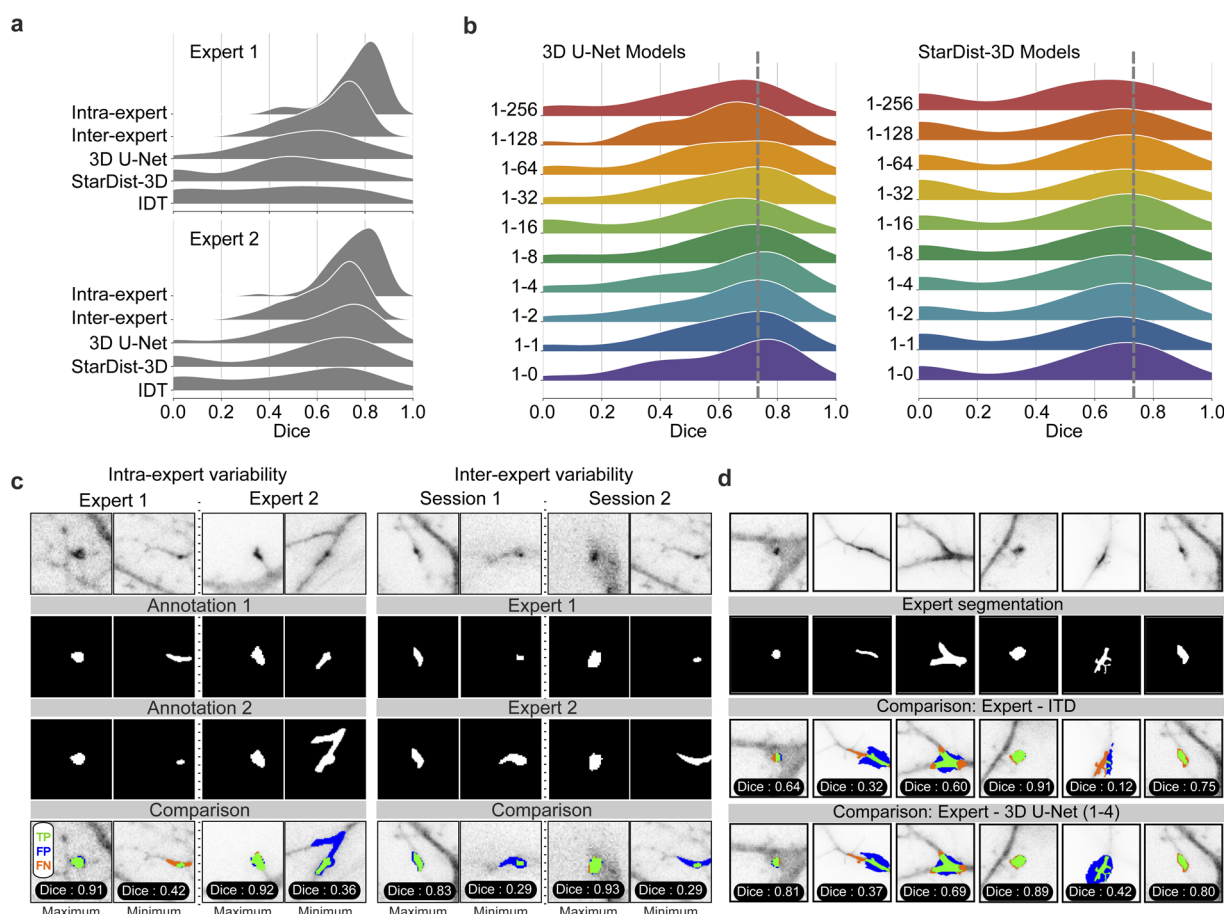


Fig. 4 Segmentation of mSCTs. (a) The segmentation performance of the models is measured on a testing dataset of 69 mSCTs (1 frame/mSCT) annotated by two experts. The segmentation masks of each mSCTs are compared to the one of each expert to account for inter-expert variability. Intra-expert agreement is evaluated using annotations from the same expert performed within a two week interval. The performance is reported for the DL models trained without negative instances (PU ratio 1–0). (b) Segmentation performance of StarDist-3D and 3D U-Net for different PU configurations. Expert 2's first annotation session is used as ground truth to measure the dice score. The 3D U-Net achieves an increased segmentation performance compared to the inter-expert agreement (distribution maximum of inter-expert agreement, gray dashed line) for PU ratios below 1–64. The best segmentation performance is obtained for a PU ratio of 1–4. (c) Example annotations (IDT) and predictions (3D U-Net with PU = 1–4) compared to the expert ground truths. (d) Comparison of expert segmentation with 3D U-Net predictions (PU = 1–4) and their dice scores.



Notably, ratios between 1–2 and 1–8 decrease the variability compared to the expert annotations: the number of segmentations with low dice scores below 0.5 decreases. As for the detection, PU learning does not improve the segmentation performance of StarDist-3D. Additionally, all StarDist-3D models show a bimodal dice distribution with first mode near zero. This indicates that StarDist-3D is unable to segment

a significant number of ground truth events, which is evocative of the large number of missed events with $\Delta F/F_0 < 1$ (Fig. 3f).

3.4 Multidimensional analysis of detected mSCTs

The presented detection and segmentation pipeline can serve as a valuable tool to extract morphology and kinetic features from mSCTs. We used the 3D U-Net trained with a PU learning ratio

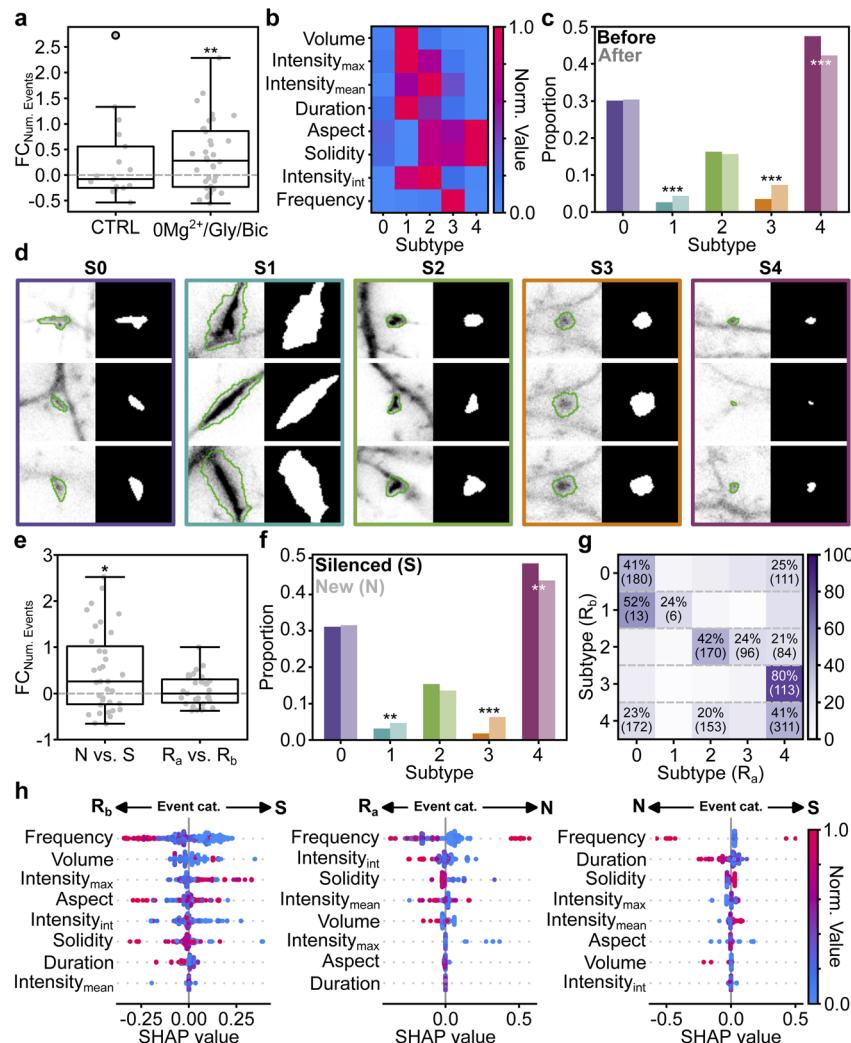


Fig. 5 Quantitative analysis of mSCT features in a cLTP paradigm. (a) The fold change in the number of detected mSCTs (FC_{Num. Events}) is significantly increased following a cLTP-inducing stimulus (0Mg²⁺/Gly/Bic; Wilcoxon Signed Rank Test: p -value = 0.009), while it remains unchanged in the control condition (CTRL; Wilcoxon Signed Rank Test: p -value = 0.644). (b) Median morphological and kinetic normalized feature values for each subtype obtained from K-means clustering (ESI Table 3† for normalization values). (c) The proportion of events belonging to each subtype is modulated by a cLTP inducing stimulus. χ^2 statistical analysis is performed (p -value = 1.63×10^{-10}) followed by a post-hoc χ^2 analysis test (S0: 8.24×10^{-1} , S1: 7.70×10^{-4} , S2: 5.35×10^{-1} , S3: 3.83×10^{-9} , S4: 2.13×10^{-4}). (d) Fluorescence signal and associated 3D U-Net segmentation for each mSCT subtype. (left) Image of detected transients at their maximal $\Delta F/F_0$ and the corresponding segmented borders (green overlay). (right) Segmentation mask predicted by the 3D U-Net for the frame with maximal $\Delta F/F_0$. Crops are $10.24 \mu\text{m} \times 10.24 \mu\text{m}$. (e) The fold change in the number of new (N) events (FC_{Num. Events}) is significantly increased compared to the number of silenced events following the cLTP stimulus (S, Wilcoxon Signed Rank Test: p -value = 0.02). The number of recurrent events is not significantly different before (R_b) and after (R_a) the stimulation (t -test: p -value = 0.30). (f) The proportion of events belonging to each subtype is differently modulated for the silenced (dark) and new events (pale). χ^2 statistical analysis is performed (p -value = 1.36×10^{-10}) followed by a post-hoc χ^2 analysis test (S0: 7.92×10^{-1} , S1: 2.15×10^{-2} , S2: 1.36×10^{-1} , S3: 6.11×10^{-11} , S4: 6.24×10^{-3}). (g) The subtypes of R_b events are associated with R_a events of different subtypes. Only $>20\%$ association are displayed. The raw number of events is shown in parenthesis. (h) SHAP value obtained on the testing dataset from a decision tree classifier trained to differentiate between event categories (R_a vs. S, R_b vs. N, and N vs. S) using the features extracted from the 3D U-Net segmentation mask for each detected mSCT (see Methods). Features are ranked according to their impact on the model's output. Events are color-coded according to their normalized feature value (same normalization as in (b)).



of 1–64 as it provides a good trade-off in detection and segmentation performance. The model was applied to the detection and segmentation of mSCTs on an unseen Ca^{2+} imaging dataset acquired on the same microscope. This dataset consists of paired videos of 600 frames, (see Methods) consisting of a baseline and a second video acquired 17 minutes after the end of the baseline video. In the control condition, the neurons were kept in a $0\text{Mg}^{2+}/\text{TTX}$ solution throughout. We tested the effect of a cLTP stimulus on mSCTs using a bath application of a $0\text{Mg}^{2+}/\text{Gly/Bic}$ solution during 7 minutes (ref. 64 and 65, see Methods) following the baseline video acquisition. The post-treatment video was acquired 10 minutes after the end of the stimulation, as in the control condition.

We observe a significant increase in the number of mSCTs following the cLTP stimulus (Fig. 5a). Seeing the heterogeneous distribution of morphology and kinetic features of mSCTs revealed by our quantitative analysis pipeline, we next extracted those features from the 3D U-Net's mSCT segmentation masks (ESI Table 2†). From all extracted features, we performed a dependency analysis to identify the most relevant features and reduce interdependence between the variables. The segmented mSCTs were clustered using the *K*-means algorithm to identify mSCT subtypes in the dataset. The number of subtypes $K = 5$ is determined using the Silhouette score and the Elbow method (ESI Fig. 5†). The median value of the features for each subtype is shown in Fig. 5b. To evaluate the effect of the cLTP treatment, we measured the proportion of mSCTs associated with each subtype before and after the cLTP stimulus (Fig. 5c). We observe that the proportion of the most prevalent subtype (subtype 4), which corresponds to round, short, and small $\Delta F/F_0$ Ca^{2+} events is significantly reduced after the stimulus. Meanwhile, the proportion of high frequency Ca^{2+} events (subtype 3), as well as of large events associated with a high $\Delta F/F_0$ (subtype 1), is significantly increased by the cLTP stimulus. Fig. 5d shows examples of the different mSCT subtypes together with the 3D U-Net's segmentation mask that were used to perform the feature analysis.

Using the spatial coordinate of the segmentation masks, we can associate mSCTs occurring in the same region at different time points and classify them as: silenced (S) when they are present only in the baseline video, new (N) for events detected only after the stimulus, and recurrent (R) for events detected in the same region before (R_b), and after (R_a) the stimulus. The increase of events following the cLTP stimulus (Fig. 5a) is supported by the emergence of new active regions (Fig. 5e). We next compared the proportion of subtypes between silenced and new events (Fig. 5f). The measured proportions closely follow the overall proportion that was measured when combining all events (Fig. 5c). To measure whether the treatment impacts the features of recurrent events differently, we associated the subtype of each R_b event with that of R_a events. As shown in Fig. 5g, associated mSCTs do not necessarily share the same subtype before and after the stimulus but stronger correspondence between specific subtypes before and after the stimulus indicates that the modulation of recurrent events is dependant on the features of the Ca^{2+} event before the cLTP treatment.

We next evaluated the importance of each feature to discriminate between the different mSCT classes (S, N, R_a , R_b). We trained

a decision tree classifier to differentiate mSCTs according to their classes, and computed the SHAP values to reveal the most important features leading to the predictions. SHAP values are also used to assess the impact that feature values have on the predicted outcome (in this case the classification task). In the SHAP value plot (Fig. 5h), the features are presented in decreasing order of importance (most important = top-most feature), and the feature values (blue data point = low value, red data point = high value) are ordered along the *x*-axis according to whether they are likely to cause the model to predict that a mSCT belongs to one class or to another class. From Fig. 5h, one can see that silenced mSCTs and new mSCTs are principally differentiated from recurrent mSCTs by their frequency. The second most important feature indicates that smaller events in the baseline videos are generally associated with silenced (S) mSCTs compared to recurrent (R_b) mSCTs. A lower integrated intensity is beneficial to differentiate between new (N) and recurrent (R_a) mSCTs in the videos acquired after the cLTP stimulus. The SHAP values also indicate that the duration of the event is useful in discriminating between S and N events, but has only little impact for the other classes (Fig. 5h). Our automated detection and segmentation approach with the 3D U-Net, combined with a multidimensional feature analysis of mSCTs showed that the increase in the event number measured following a cLTP-inducing stimulus is supported by the appearance of new active regions. Those new regions have distinct features, among which the proportion of events with high frequency is significantly increased, while small and short events are reduced following the stimulus.

4 Discussion

Through the application of PU learning to the quantitative analysis of Ca^{2+} imaging data, we have provided accurate detection and segmentation of mSCTs in fluorescence microscopy videos. We could extract signal dynamics and meaningful morphological features from these heterogeneous, low density (both spatial and temporal), low intensity, and propagating events. We have demonstrated that the use of unlabeled instances in a PU learning framework can improve the performance for the detection of low intensity Ca^{2+} that are missed by other approaches, including other DL methods using solely positive examples for training. The improved performance observed with the 3D U-Net models was achieved simply by adding low-cost, quickly-sampled unlabeled instances to the existing positive instances. The training pipeline is implemented in an easy-to-use ZeroCostDL4Mic Jupyter notebook enabling straightforward training and fine-tuning of the models on new datasets, and specific use cases.⁶³

We further showed that our approach allows the extraction of features from the segmentation masks to measure the effect of a cLTP stimulus on mSCT morphologies and dynamics. The Ca^{2+} events extracted from the 3D U-Net detection and segmentation pipeline could be clustered into 5 main subtypes, that are differently modulated by the cLTP protocol. Having access to precise spatio-temporal localization of the mSCTs revealed that such cLTP stimulus leads largely to the emergence of new active regions, rather than an increase in the frequency of events within regions already active prior to the stimulus.



This result may reflect a form of plasticity that is part of the mechanisms supporting long term potentiation of synaptic transmission.^{66,67} This potentiation may reflect changes in release probability in some axonal terminals,^{68,69} increase recruitment of Ca^{2+} permeable ion channels in post-synaptic regions,^{70,71} or an increase coupling between receptor activation and Ca^{2+} store release.^{4,72} The ability to identify and analyze localized regions of activity will allow to dissect these various mechanisms and correlate them with molecular trafficking of proteins, such as the Ca^{2+} /Calmodulin-Protein kinase II,⁷³ or cytoskeletal remodelling of dendritic actin filaments.⁶⁴

Using the segmentation masks, we could also train a decision tree classifier to discriminate between events depending on the moment they were detected (before or after stimulation). SHAP values provided better insights into which features predominantly influence the model's predictions, revealing that different features are used to distinguish recurrent events from new and silenced events.

The robustness and generalization capacities of our method were also highlighted through its application for the detection and segmentation of mSCTs on an unseen Ca^{2+} imaging dataset acquired with a different microscope. The performance of the 3D U-Net model was maintained on this out-of-distribution dataset. We also showed that the PU learning setting was also beneficial for the generalization. The presented method should be readily applicable to many other small datasets of Ca^{2+} imaging, in which the events of interest are sparse and heterogeneous, providing insight into different applications and biological inquiries. For instance, this could be applied to the detection of dopamine or norepinephrine dynamics using the GPCR-activation-based (GRAB) sensors^{74,75} or local glutamate release using the iGluSnFR sensor.⁷⁶ We also showed that it can be applied to datasets with missing ground truth annotations, and still provide improvement on these annotations through the PU training of the networks, enabling better modeling of the boundaries between real Ca^{2+} transients and foreground signal fluctuations. While we have considered a simple formulation of PU learning, it could also be of interest to consider more sophisticated definitions such as in Wolny *et al.*³² on a variety of bio-imaging datasets. Integration of the DL models into an accessible platform such as ZeroCostDL4Mic⁶³ should also facilitate the application of the proposed framework to new datasets or using other annotation methods as ground truths for training.

Code availability

All code used in this manuscript are open source and available at: <https://github.com/FLClab/Calcium-Analysis>. The ZeroCostDL4Mic notebook allows users to train, finetune, and predict on their own dataset. Optionally, the notebook provides a subset of data from this manuscript.

Data availability

All datasets used to train the models and the corresponding acquired images are available for download at <https://s3.valeria.science/flclab-calcium/index.html>.

Author contributions

F. B., A. B., G. L., R. H., C. G., and F. L. C. designed the deep learning analysis strategy. T. W., M. L., and P. D. K. designed the Ca^{2+} imaging experiments. T. W. performed the Ca^{2+} imaging experiments. S. L. developed the Ca^{2+} imaging acquisition software. T. W., M. L., S. L., and G. N. developed the IDT approach. A. B., F. B., and F. L. C. designed the multidimensional analysis approach. T. W. and G. L. designed the user-study. T. W., G. L., and F. L. C. annotated the testing datasets. K. C. and B. L. F. tested implementations of IDT and PU learning strategies. F. B. and A. B. implemented the deep learning models, performed the PU learning experiments, and analyzed the results. F. B., A. B., and F. L. C. wrote the manuscript. R. H., P. D. K., C. G., and F. L. C. co-supervised the project.

Conflicts of interest

The authors declare no competing interests.

Acknowledgements

We acknowledge the Neuronal Cell Culture Platform of the CERVO Brain Research Center for the preparation of the dissociated hippocampal cultures. We thank Annette Schwerdtfeger for careful proofreading of the manuscript. Funding was provided by grants from the Natural Sciences and Engineering Research Council of Canada (NSERC) (RGPIN-2019-06704 to F.L.C., RGPIN-2017-06171 to P. D. K. RGPIN-2018-05750 to R. H.), Fonds de Recherche Nature et Technologie (FRQNT) Team Grant (2021-PR-284335 to F. L. C, C. G. and P. D. K.), the Canadian Institute for Health Research (CIHR) (471107 to F. L. C. and P. D. K.), a New Frontiers in Research Fund Exploration Grant (NFRFE-2020-00933 to F. L. C., C. G. and R. H.), and the Neuronex Initiative (National Science Foundation 2014862, Fonds de recherche du Québec – Santé 295824 to F. L. C. and P. D. K.). R. H. acknowledges support from CIFAR, the Azrieli and Alfred. P. Sloan foundations and the Connaught Fund. C. G. is a CIFAR AI-Chair and F. L. C. is a Canada Research Chair Tier II. A. B. was supported by a scholarship from NSERC. F. B. was supported by scholarships from FRQNT, NeuroQuébec, and the Québec Bio-Imaging Network. A. B., F. B., and T. W. were awarded an excellence scholarship from the FRQNT strategic cluster UNIQUE.

Notes and references

- 1 J. N. Kerr and W. Denk, *Nat. Rev. Neurosci.*, 2008, **9**, 195–205.
- 2 C. Grienberger and A. Konnerth, *Neuron*, 2012, **73**, 862–885.
- 3 T. H. Murphy, J. M. Baraban and W. G. Wier, *Neuron*, 1995, **15**, 159–168.
- 4 K. F. Lee, C. Soares, J.-P. Thivierge and J.-C. Béïque, *Neuron*, 2016, **89**, 784–799.
- 5 Y. Zhang, M. Rózsa, Y. Liang, D. Bushey, Z. Wei, J. Zheng, D. Reep, G. J. Broussard, A. Tsang, G. Tsegaye, *et al.*, *Nature*, 2023, **615**, 884–891.



6 T.-W. Chen, T. J. Wardill, Y. Sun, S. R. Pulver, S. L. Renninger, A. Baohan, E. R. Schreiter, R. A. Kerr, M. B. Orger, V. Jayaraman, *et al.*, *Nature*, 2013, **499**, 295–300.

7 M. Inoue, A. Takeuchi, S. Manita, S.-i. Horigane, M. Sakamoto, R. Kawakami, K. Yamaguchi, K. Otomo, H. Yokoyama, R. Kim, *et al.*, *Cell*, 2019, **177**, 1346–1360.

8 A. L. Reese and E. T. Kavalali, *eLife*, 2016, **5**, e21170.

9 E. T. Kavalali, *Nat. Rev. Neurosci.*, 2015, **16**, 5–16.

10 L. C. Andreae and J. Burrone, *Cell Rep.*, 2015, **10**, 873–882.

11 A. S. Walker, G. Neves, F. Grillo, R. E. Jackson, M. Rigby, C. O'Donnell, A. S. Lowe, G. Vizcay-Barrena, R. A. Fleck and J. Burrone, *Proc. Natl. Acad. Sci. U. S. A.*, 2017, **114**, E1986–E1995.

12 V. N. Murthy, T. J. Sejnowski and C. F. Stevens, *Proc. Natl. Acad. Sci. U. S. A.*, 2000, **97**, 901–906.

13 I. J. Park, Y. V. Bobkov, B. W. Ache and J. C. Principe, *J. Neurosci. Methods*, 2013, **218**, 196–205.

14 E. Yaksi and R. W. Friedrich, *Nat. Methods*, 2006, **3**, 377–383.

15 A. Giovannucci, J. Friedrich, P. Gunn, J. Kalfon, B. L. Brown, S. A. Koay, J. Taxidis, F. Najafi, J. L. Gauthier, P. Zhou, B. S. Khakh, D. W. Tank, D. B. Chklovskii and E. A. Pnevmatikakis, *eLife*, 2019, **8**, e38173.

16 M. Pachitariu, C. Stringer, M. Dipoppa, S. Schröder, L. F. Rossi, H. Dalgleish, M. Carandini and K. D. Harris, Suite2p: Beyond 10,000 Neurons with Standard Two-Photon Microscopy, *bioRxiv*, 2017, DOI: [10.1101/061507](https://doi.org/10.1101/061507).

17 A. Agarwal, P.-H. Wu, E. G. Hughes, M. Fukaya, M. A. Tischfield, A. J. Langseth, D. Wirtz and D. E. Bergles, *Neuron*, 2017, **93**, 587–605.

18 R. Srinivasan, B. S. Huang, S. Venugopal, A. D. Johnston, H. Chai, H. Zeng, P. Golshani and B. S. Khakh, *Nat. Neurosci.*, 2015, **18**, 708–717.

19 Y. Wang, N. V. DelRosso, T. V. Vaidyanathan, M. K. Cahill, M. E. Reitman, S. Pittolo, X. Mi, G. Yu and K. E. Poskanzer, *Nat. Neurosci.*, 2019, **22**, 1936–1944.

20 O. Ronneberger, P. Fischer and T. Brox, *Medical Image Computing and Computer-Assisted Intervention–MICCAI 2015: 18th International Conference, Munich, Germany, October 5–9, 2015, Proceedings, Part III* 18, 2015, pp. 234–241.

21 Y. Xu, F. Gao, T. Wu, K. M. Bennett, J. R. Charlton and S. Sarkar, *2019 IEEE 15th International Conference on Automation Science and Engineering (CASE)*, 2019, pp. 1761–1767.

22 P. Ma, C. Li, M. M. Rahaman, Y. Yao, J. Zhang, S. Zou, X. Zhao and M. Grzegorzek, *Artif. Intell. Rev.*, 2023, **56**, 1627–1698.

23 A. Klibisz, D. Rose, M. Eicholtz, J. Blundon and S. Zakharenko, *Deep Learning in Medical Image Analysis and Multimodal Learning for Clinical Decision Support: Third International Workshop, DLMIA 2017, and 7th International Workshop, ML-CDS 2017, Held in Conjunction with MICCAI 2017, Québec City, QC, Canada*, 2017, pp. 285–293.

24 L. Sità, M. Brondi, P. Lagomarsino de Leon Roig, S. Curreli, M. Panniello, D. Vecchia and T. Fellin, *Nat. Commun.*, 2022, **13**, 1529.

25 S. Soltanian-Zadeh, K. Sahingur, S. Blau, Y. Gong and S. Farsiu, *Proc. Natl. Acad. Sci. U. S. A.*, 2019, **116**, 8554–8563.

26 N. Ruffini, S. Altahini, S. Weißbach, N. Weber, J. Milkovits, A. Wierczeiko, H. Backhaus and A. Stroh, *Bioinformatics*, 2024, **40**, btae177.

27 Z. Xu, Y. Wu, J. Guan, S. Liang, J. Pan, M. Wang, Q. Hu, H. Jia, X. Chen and X. Liao, *Front. Cell. Neurosci.*, 2023, **17**, 1127847.

28 L. Alzubaidi, J. Zhang, A. J. Humaidi, A. Al-Dujaili, Y. Duan, O. Al-Shamma, J. Santamaría, M. A. Fadhel, M. Al-Amidie and L. Farhan, *J. Big Data*, 2021, **8**, 1–74.

29 A. Bilodeau, C. V. L. Delmas, M. Parent, P. De Koninck, A. Durand and F. Lavoie-Cardinal, *Nat. Mach. Intell.*, 2022, **4**, 455–466.

30 E. Gómez-de-Mariscal, M. Maška, A. Kotrbová, V. Pospíchalová, P. Matula and A. Muñoz-Barrutia, *Sci. Rep.*, 2019, **9**, 13211.

31 J. Bekker and J. Davis, *Mach. Learn.*, 2020, **109**, 719–760.

32 A. Wolny, Q. Yu, C. Pape and A. Kreshuk, *Proceedings of the IEEE/CVF Conference on Computer Vision and Pattern Recognition*, 2022, pp. 4402–4411.

33 F. Denis, R. Gilleron and F. Letouzey, *Theor. Comput. Sci.*, 2005, **348**, 70–83.

34 F. Chen, S. Li, C. Wei, Y. Zhang, K. Guo, Y. Zheng, F. Cao and J. Liang, *Biomed. Signal Process. Control*, 2024, **87**, 105473.

35 L. Lejeune and R. Sznitman, *Med. Image Anal.*, 2021, **73**, 102185.

36 Ö. Çiçek, A. Abdulkadir, S. S. Lienkamp, T. Brox and O. Ronneberger, 3D U-Net: learning dense volumetric segmentation from sparse annotation, in *Medical Image Computing and Computer-Assisted Intervention–MICCAI 2016: 19th International Conference, Proceedings, Part II* 19, Springer International Publishing, Athens, Greece, 2016, pp. 424–432.

37 Ö. Çiçek, A. Abdulkadir, S. S. Lienkamp, T. Brox and O. Ronneberger, *arXiv*, preprint, arXiv:1606.06650 cs, 2016.

38 M. Weigert, U. Schmidt, R. Haase, K. Sugawara and G. Myers, *2020 IEEE Winter Conference on Applications of Computer Vision (WACV)*, Snowmass Village, CO, USA, 2020, pp. 3655–3662.

39 P. Dotti, M. Fernandez-Tenorio, R. Janicek, P. Márquez-Neila, M. Wullschleger, R. Sznitman and M. Egger, *Cell Calcium*, 2024, 102893.

40 A. Hudmon, E. LeBel, H. Roy, A. Sik, H. Schulman, M. N. Waxham and P. De Koninck, *J. Neurosci.*, 2005, **25**, 6971–6983.

41 F. Nault and P. De Koninck, *Protocols for Neural Cell Culture: Fourth Edition*, 2010, pp. 137–159.

42 W.-Y. Lu, H.-Y. Man, W. Ju, W. S. Trimble, J. F. MacDonald and Y. T. Wang, *Neuron*, 2001, **29**, 243–254.

43 M. Gralle, S. Labrecque, C. Salesse and P. De Koninck, *J. Neurochem.*, 2021, **156**, 88–105.

44 M. Guizar-Sicairos, S. T. Thurman and J. R. Fienup, *Opt. Lett.*, 2008, **33**, 156–158.

45 S.-J. Baek, A. Park, Y.-J. Ahn and J. Choo, *Analyst*, 2015, **140**, 250–257.

46 H. Dana, B. Mohar, Y. Sun, S. Narayan, A. Gordus, J. P. Hasseman, G. Tsegaye, G. T. Holt, A. Hu, D. Walpita, *et al.*, *elife*, 2016, **5**, e12727.



47 A. Paszke, S. Gross, F. Massa, A. Lerer, J. Bradbury, G. Chanan, T. Killeen, Z. Lin, N. Gimelshein, L. Antiga, A. Desmaison, A. Köpf, E. Yang, Z. DeVito, M. Raison, A. Tejani, S. Chilamkurthy, B. Steiner, L. Fang, J. Bai and S. Chintala, PyTorch: An Imperative Style, High-Performance Deep Learning Library, *Proceedings of the 33rd International Conference on Neural Information Processing Systems*, 2019, pp. 8026–8037.

48 U. Schmidt, M. Weigert, C. Broaddus and G. Myers, Cell detection with star-convex polygons, in *Medical Image Computing and Computer Assisted Intervention–MICCAI 2018: 21st International Conference*, Proceedings, Part II 11, Springer International Publishing, Granada, Spain, 2018, pp. 265–273.

49 A. Hatamizadeh, D. Yang, H. Roth and D. Xu, *CVF Winter Conference on Applications of Computer Vision (WACV)*, 2021, pp. 1748–1758.

50 M. J. Cardoso, W. Li, R. Brown, N. Ma, E. Kerfoot, Y. Wang, B. Murrey, A. Myronenko, C. Zhao, D. Yang, *et al.*, *arXiv*, 2022, preprint, arXiv:2211.02701, DOI: [10.48550/arXiv.2211.02701](https://doi.org/10.48550/arXiv.2211.02701).

51 O. Oktay, J. Schlemper, L. L. Folgoc, M. Lee, M. Heinrich, K. Misawa, K. Mori, S. McDonagh, N. Y. Hammerla, B. Kainz and B. Glocker, *Medical Imaging with Deep Learning 2018 (MIDL2018)*, 2018.

52 Y. LeCun, Y. Bengio and G. Hinton, *Nature*, 2015, **521**, 436–444.

53 S. Azizi, L. Culp, J. Freyberg, B. Mustafa, S. Baur, S. Kornblith, T. Chen, N. Tomasev, J. Mitrović, P. Strachan, S. S. Mahdavi, E. Wulczyn, B. Babenko, M. Walker, A. Loh, P.-H. C. Chen, Y. Liu, P. Bavishi, S. M. McKinney, J. Winkens, A. G. Roy, Z. Beaver, F. Ryan, J. Krogue, M. Etemadi, U. Telang, Y. Liu, L. Peng, G. S. Corrado, D. R. Webster, D. Fleet, G. Hinton, N. Houlsby, A. Karthikesalingam, M. Norouzi and V. Natarajan, *Nat. Biomed. Eng.*, 2023, **7**, 756–779.

54 H. W. Kuhn, *Nav. Res. Logist. Q.*, 1955, **2**, 83–97.

55 L. R. Dice, *Ecology*, 1945, **26**, 297–302.

56 P. J. Rousseeuw, *J. Comput. Appl. Math.*, 1987, **20**, 53–65.

57 R. L. Thorndike, *Psychometrika*, 1953, **18**, 267–276.

58 S. van der Walt, J. L. Schönberger, J. Nunez-Iglesias, F. Boulogne, J. D. Warner, N. Yager, E. Gouillart, T. Yu and the scikit-image contributors, *PeerJ*, 2014, **2**, e453.

59 F. Pedregosa, G. Varoquaux, A. Gramfort, V. Michel, B. Thirion, O. Grisel, M. Blondel, P. Prettenhofer, R. Weiss, V. Dubourg, J. Vanderplas, A. Passos, D. Cournapeau, M. Brucher, M. Perrot and E. Duchesnay, *J. Mach. Learn. Res.*, 2011, **12**, 2825–2830.

60 S. M. Lundberg and S.-I. Lee, *Advances in Neural Information Processing Systems 30*, Curran Associates, Inc., 2017, pp. 4765–4774.

61 F. Wilcoxon, *Biom. Bull.*, 1945, **1**, 80–83.

62 S. S. Shapiro and M. B. Wilk, *Biometrika*, 1965, **52**, 591–611.

63 L. von Chamier, R. F. Laine, J. Jukkala, C. Spahn, D. Krentzel, E. Nehme, M. Lerche, S. Hernández-Pérez, P. K. Mattila, E. Karinou, *et al.*, *Nat. Commun.*, 2021, **12**, 2276.

64 F. Lavoie-Cardinal, A. Bilodeau, M. Lemieux, M.-A. Gardner, T. Wiesner, G. Laramée, C. Gagné and P. De Koninck, *Sci. Rep.*, 2020, **10**, 11960.

65 T. Wiesner, A. Bilodeau, R. Bernatchez, A. Deschênes, B. Raulier, P. De Koninck and F. Lavoie-Cardinal, *Front. Neural Circuits*, 2020, **14**, 57.

66 E. Edelmann, E. Cepeda-Prado and V. Leßmann, *Front. Synaptic Neurosci.*, 2017, **9**, 7.

67 A. Citri and R. C. Malenka, *Neuropsychopharmacology*, 2008, **33**, 18–41.

68 J. H. Jung, L. M. Kirk, J. N. Bourne and K. M. Harris, *Proc. Natl. Acad. Sci.*, 2021, **118**, e2018653118.

69 P. E. Castillo, *Cold Spring Harbor Perspect. Biol.*, 2012, **4**, a005728.

70 A. J. Watt, M. C. Van Rossum, K. M. MacLeod, S. B. Nelson and G. G. Turrigiano, *Neuron*, 2000, **26**, 659–670.

71 P. Park, H. Kang, T. M. Sanderson, Z. A. Bortolotto, J. Georgiou, M. Zhuo, B.-K. Kaang and G. L. Collingridge, *Front. Synaptic Neurosci.*, 2018, **10**, 42.

72 A. L. Reese and E. T. Kavalali, *Elife*, 2015, **4**, e09262.

73 M. Lemieux, S. Labrecque, C. Tardif, É. Labrie-Dion, É. LeBel and P. De Koninck, *J. Cell Biol.*, 2012, **198**, 1055–1073.

74 J. Feng, C. Zhang, J. E. Lischinsky, M. Jing, J. Zhou, H. Wang, Y. Zhang, A. Dong, Z. Wu, H. Wu, *et al.*, *Neuron*, 2019, **102**, 745–761.

75 F. Sun, J. Zhou, B. Dai, T. Qian, J. Zeng, X. Li, Y. Zhuo, Y. Zhang, Y. Wang, C. Qian, *et al.*, *Nat. Methods*, 2020, **17**, 1156–1166.

76 J. S. Marvin, B. G. Borghuis, L. Tian, J. Cichon, M. T. Harnett, J. Akerboom, A. Gordus, S. L. Renninger, T.-W. Chen, C. I. Bargmann, *et al.*, *Nat. Methods*, 2013, **10**, 162–170.

